Image segmentation based on an active contour model of partial image restoration with local cosine fitting energy

Jiaqing Miao [a,b], Ting-Zhu Huang [a,*], Xiaobing Zhou [b,*], Yugang Wang [a], Jun Liu [a]

[a] *School of Mathematical Sciences/Institute of Computational Science, University of Electronic Science and Technology of China, Chengdu, Sichuan 611731, PR China*
[b] *Department of Geophysical Engineering, Montana Tech of The University of Montana, Butte, MT 59701, USA*

ARTICLE INFO

ABSTRACT

In this paper, we use the cosine function to express the data energy fitting of a traditional active contours model and propose a model based on sectional image recovery local cosine-fitting energy active contours, which is used to segment medical and synthetic images. The algorithm is a single level image segmentation method. It can process synthetic images with intensity inhomogeneity. Moreover, our model for the images with noise and the fuzzy ones is more efficient and robust, and the computational speed was similar or faster, compared with Convex Variant of the Mumford–Shah Model and Thresholding (CVMST) model, a local binary fitting (LBF) model and L_0 Regularized Mumford–Shah (L0MS) model. In addition, we describe the model in a discrete form, which is more convenient to add a regular term to control the segmentation. Therefore the massive calculation is reduced by re-initializing the level set curve. At the end of the paper, the modified algorithm has been utilized to segment medical images and three-dimensional visualization results are obtained. The experimental results indicate that the segmentation results are accurate and efficient when applied to different kinds of images.

© 2018 Elsevier Inc. All rights reserved.

1. Introduction

Image segmentation is an important research subject in the image processing. The active contour model is one of the most important algorithms in image segmentation [3,4]. It can be divided into two types: the edge-based models and the region-based models, depending on either the edge or the gradient information is used to drive the contours to identify the boundaries of the expected objects [26]. In practice, these models can effectively segment images with strong boundaries, but fail to detect objects with weak boundaries. Their success depends on the initial contour and is sensitive to noises. Compared with the edge-based models [24], the region-based models use the regional statistic information to control the change of active contours. Thus, they outperform the edge-based models and are less sensitive to the initial contour and noises. Hence, in this study, we mainly focus on the region-based models. Osher and Sethian [22] proposed an image segmentation method based on active contours level set. The main idea of the level set method is to express a curve by a zero-level set with a high dimensional function, also called a level set function (LSF) [1,12,13,20]. Then the evolution of the

---

* Corresponding authors.
E-mail addresses: jmiao@mtech.edu, mjq_011114117@163.com (J. Miao), tzhuang@uestc.edu.cn, tingzhuhuang@126.com (T.-Z. Huang), xzhou@mtech.edu (X. Zhou).

curve corresponds to the improved function. In this way we do not need to change the topological structure of the LSF. The change in the topological structure of the curve can be controlled by improving the zero-level set of the LSF.

At present, several models commonly used are restricted in many practical cases. They fail to segment images with strong noises and intensity inhomogeneity. Intensity inhomogeneity exists ubiquitously in real images. Therefore, it is quite necessary to develop new methods that can segment these images efficiently. A local binary fitting (LBF) model [16,17] has been introduced, which is suitable for segmenting images with intensity inhomogeneity. The LBF model takes advantage of the region technology and intensity information.

In this study, we propose a new model of region active contours that is based on the sectional recovery updating. A cosine function is used to express the data fitting energy in this model [34]. At the same time, inspired by the LBF model, in order to get more information from the original image with intensity inhomogeneity we utilize the local image information. Results show that our model can recover problematic images of different types. Our model is more efficient and accurate, compared with the Mumford–Shah (M–S) model, Chan–Vese (C–V) model, LBF model, Convex Variant of the M–S Model and Thresholding (CVMST) model, and L_0 Regularized M–S (L0MS) model.

2. Background

The M–S, C–V, CVMST, LBF, and L0MS models are commonly used for image segmentation. The technology of the single-level set and multiple-level set methods of segmentation technology has been improved based on these models.

2.1. The M–S model

Mumford and Shah [21] proposed an energy functional model of level set image segmentation using the function optimization method for image segmentation. This model is simply referred to as the M–S model. One remarkable characteristic of the M–S model is its overall optimization, which uses a closed initial curve to successfully detect objects with a concave boundary and its inside with cave. Meanwhile it can work well without any specialized processing. The initial curve does not have to be inside or outside completely of the homogeneous region. It can distinguish correctly the object region and the background region. Another characteristic of this model is its independence on the edge information of the image. Therefore, even if the edge is fuzzy or discretized, it can still achieve the desired effect. In 1989, they proposed a method again that solved the edge detection problem by a piecewise smooth function. In the past 20 years, there are many achievements in the application of the M–S model, such as image restoration, noise cancellation, image segmentation, and shape matching. Let I be an image and Ω its domain. We assume that C, the boundary of the image, divides the I into several homogeneous regions. Then we can obtain the segmentation image I_0. The M–S model searches the actual edge C_0 of the image. In order to divide the image I into several homogeneous regions, we firstly define the piecewise smooth function of the approximately minimized energy functional model as follows:

$$E_{MS}(I_0, C) = \frac{\lambda}{2} \int_{\Omega} (I - I_0)^2 dx + \frac{\mu}{2} \int_{\Omega \backslash C} |\nabla I_0|^2 dx + Length(C), \tag{1}$$

where I is an input image, I_0 the output image to optimize, μ a positive parameter, and C the approximately continuous closed curve of the image edge only in the $\Omega \backslash C$ domain. $|\nabla I_0|^2 = (\frac{\partial I_0}{\partial x})^2 + (\frac{\partial I_0}{\partial y})^2$ is the sum of the square of the gradient components of I_0. The first term in Eq. (1) is the energy term to be minimized, the second term is a smoothing term for any area except for the boundary C, and the third term is the length-controlling term.

We can segment an image by solving the above minimum-value problem without the necessity to preprocess (e.g. denoising) the image before segmentation. The model does not depend on the gradient and other edge information. Thus, the weak edges of objects of interest within an image can be recognized through the boundary smoothing and can be segmented accurately. However, the model is non-convex so it may not converge to a global extremum, especially at the concavities or turning points of the gray level image. During the process of energy minimization, the rate of convergence may be slow or the numerical value is not stable.

2.2. The C–V model

Chan and Vese [6,28] proposed a novel active contours model, which is a special case of the M–S function. This model is briefed as the C–V model. In the C–V model the procedure of image segmentation is as follows: given an image I, we find a contour C dividing the image into two regions: *inside(c)* and *outside(c)* regions. At the same time, we use constants c_1 and c_2 to approximate the average gray values of the two regions, and define the energy functional of the C–V model as follows:

$$\begin{aligned} E(c_1, c_2, C) = &\lambda_1 \int_{inside(c)} |I(x) - c_1|^2 dx + \lambda_2 \int_{outside(c)} |I(x) - c_2|^2 dx \\ &+ \mu \cdot Length(C) + \nu \cdot Area(inside(C)) \end{aligned} \tag{2}$$

where $\mu \geq 0$, $\nu \geq 0$, λ_1, $\lambda_2 > 0$ are constant parameters. Then we substitute the energy functional into the level set formulation to obtain the following equation:

$$
\begin{aligned}
E^{CV}(c_1, c_2, \phi) = & \lambda_1 \int |I(x) - c_1|^2 H(\phi(x))dx + \lambda_2 \int |I(x) - c_2|^2 (1 - H(\phi(x)))dx \\
& + \mu \int \delta(\phi)|\nabla\phi(x)|dx + \nu \int H(\phi(x))dx,
\end{aligned}
\tag{3}
$$

where, ϕ is the level set function. $H(\phi)$ and $\delta(\phi)$ are the Heaviside and Dirac functions, respectively. c_1 and c_2 can be obtained using the following equation:

$$
c_1(\phi) = \frac{\int I(x)H(\phi(x))dx}{\int H(\phi(x))dx}, \quad c_2(\phi) = \frac{\int I(x)(1 - H(\phi(x)))dx}{\int (1 - H(\phi(x)))dx},
\tag{4}
$$

When the input image is a piecewise-constant image, the C–V model can achieve good results. However, as the model uses the global information, the C–V model cannot handle well an image with intensity inhomogeneity, and cannot segment images that are strongly affected by noises either.

2.3. The LBF model

Li et al. [16,17] proposed a LBF model, which uses local information to segment images with intensity inhomogeneity. Given an image I, we can find a contour C dividing an image into two regions: the *inside(c)* and *outside(c)* regions. The LBF model is represented by the following minimized energy functional:

$$
\begin{aligned}
E(C, f_1(x), f_2(x)) = & \lambda_1 \int \left[\int_{inside(c)} K_\sigma(x-y)|I(y) - f_1(x)|^2 dy \right]dx \\
& + \lambda_2 \int \left[\int_{outside(c)} K_\sigma(x-y)|I(y) - f_2(x)|^2 dy \right]dx,
\end{aligned}
\tag{5}
$$

where λ_1 and λ_2 are positive parameters and K_σ is the Gaussian kernel with standard deviation σ. We use a level set function to represent the curve C and then we can get:

$$
\begin{aligned}
E^{LBF}(\phi, f_1, f_2) = & \lambda_1 \int \left[\int K_\sigma(x-y)|I(y) - f_1(x)|^2 H(\phi(y))dy \right]dx \\
& + \lambda_2 \int \left[\int K_\sigma(x-y)|I(y) - f_1(x)|^2 (1 - H(\phi(y)))dy \right]dx,
\end{aligned}
\tag{6}
$$

where ϕ is the level set function. $f_1(x)$ and $f_2(x)$ can be obtained from the following equations:

$$
f_1(x) = \frac{K_\sigma(x) * [H(\phi(x))I(x)]}{K_\sigma(x) * H(\phi(x))},
\tag{7}
$$

$$
f_2(x) = \frac{K_\sigma(x) * [(1 - H(\phi(x)))I(x)]}{K_\sigma(x) * (1 - H(\phi(x)))},
\tag{8}
$$

where $*$ is the convolution operator. As we use local information to introduce the Gaussian kernel, the LBF model can segment images with intensity inhomogeneity. In fact, the LBF model uses functions $f_1(x)$ and $f_2(x)$ as the local weighted average of the curve C inside and outside the Gaussian mask, respectively.

2.4. The CVMST model

Cai et al. [2] proposed a two-step segmentation model that is called CVMST model and found a method to solve the convexification problem of the M–S model. It is a convex relaxation method. The idea of the method is to minimize the segmentation tasks of the M–S function:

1) First, finding a smooth solution to the convexification problem in the M–S model;
2) Then, using a threshold to distinguish different features and to segment images.

The main task of this method aims at convex minimization of the nonconvex problem, obtaining segmentation results by the soft-threshold process. The convexification problem of the M–S model is solved by the following minimized energy functional model in the first step:

$$
\inf_{g \in W^{1,2}(\Omega)} E(g) = \inf_{g \in W^{1,2}(\Omega)} \left\{ \frac{\lambda}{2} \int_\Omega (f - Ag)^2 dx + \frac{\mu}{2} \int_\Omega |\nabla g|^2 dx + \int_\Omega |\nabla g| dx \right\},
\tag{9}
$$

where A expresses the identity operator or the fuzzy operator, and $W^{1, 2}(\Omega)$ is the Sobolev space. If $\mu \neq 0$, then g is smooth. The discrete model in equation (9) can be expressed as follows:

$$\min_{g} \left\{ \frac{\lambda}{2} \|f - Ag\|_2^2 + \frac{\mu}{2} \|\nabla g\|_2^2 + \|\nabla g\|_1 \right\},$$

(10)

In formula (10), $\|\nabla g\|_1 = \sum_{i \in \Omega} \sqrt{(\nabla_x g)_i^2 + (\nabla_y g)_i^2}$ is the classical discrete total variation (TV) norm. Although CVMST is a preferable segmentation model, it cannot process images with intensity inhomogeneity.

2.5. The L0MS model

Duan et al. [8] proposed a two-step segmentation model that is based on the L_0 norm, i.e. the L0MS model. It is a modified model of the CVMST model and uses the L_0 norm to sharpen the edges of objects. Meanwhile, this model has a good performance in processing images with intensity inhomogeneity. Firstly, we express the model in the following form:

$$F = UW,$$

(11)

where U is the image intensity, and W is the biased intensity field. Let us transform the image into the logarithm region:

$$f = \ln(F), u = \ln(U), w = \ln(W).$$

(12)

Using the logarithms (f, u and w) of F, U, and W to build an image segmentation model, the specific form is expressed as formulation (13):

$$\min_{u,w} \quad \frac{1}{2} \varepsilon(u, w) + a \|\nabla u\|_0 + \frac{\mu}{2} \|\nabla w\|^2 + \frac{\gamma}{2} \|w\|^2,$$

(13)

where

$$\varepsilon(u, w) = \sum_{p \in \Omega} \left(\sum_{q \in N_p} K(x_p - x_q)(f_q - u_q - w_p)^2 \right),$$

(14)

and a, μ, γ are regularization parameters. Although this model performs well for images with intensity inhomogeneity and intensity-corrected (homogeneous) images can be obtained, a portion of details can be lost because of the logarithm transformation. This algorithm applies also to images with noises. However, medical images, especially magnetic resonance imaging (MRI) images, are more or less affected by all kinds of noises. Due to using L_0 norm, it makes the edge too sharp, which is also one of the shortcomings of the algorithm.

3. Development of a new model

In this study, we propose a new algorithm and compare it with the above LBF, CVMST, and L0MS algorithms. The advantages of the new algorithm will be demonstrated through the numerical experiments. In this section, we use the cosine function [14,34,35] that is widely used in traditional models to express the data energy fitting and then propose a partial image restoration with the local cosine-fitting energy model (IRLCF) that is based on the image-updating strategy. The algorithm is a single-level set image segmentation method.

3.1. Symbols in the discrete form

Firstly, we define some symbols in discrete state [8]. We use matrix R to represent a grayscale image of $M \times N$ in size. Let $\Omega \subset R^2$ be the domain of an image and the space V denotes the set of R. Therefore $Q = V \times V$ if $u \in V$ and the gradient ∇u of an image u in discrete state can be expressed as follows:

$$\nabla(u_{i,j}) = (\partial_x u_{i,j}, \partial_y u_{i,j}) = (u_{i+1,j} - u_{i,j}, u_{i,j+1} - u_{i,j}),$$

(15)

where ∇ is the gradient operator with the periodic boundary condition, i is the row number, and j is the column number of a pixel (i, j). If $n = (n_1^1, n^2) \in Q$, where n is a vector in the space Q, each component is a matrix of $M \times N$, the discrete divergence $div(n_{i,j})$ can be defined as follows:

$$div(n_{i,j}) = -(\partial_x^* n_{i,j}^1 + \partial_y^* n_{i,j}^2),$$

(16)

where ∂_x^* and ∂_y^* represent the adjoint operators of ∂_x and ∂_y respectively. We define Δ as the Laplace operator of $V \to V$ and as to $u \in V$,

$$\Delta(u_{i,j}) = -(\partial_x^* \partial_x u_{i,j} + \partial_y^* \partial_y u_{i,j}),$$

(17)

Similar, we define a vector norm in discrete state, as to $\forall G \in \Omega$. We define the following norm:

$$\|u\|_G = \left(\sum_{p \in G} |u_p|^2 \right)^{\frac{1}{2}},$$

(18)

If $G = \Omega$, we can simplify the norm to $\|u\|$.

3.2. A model based on partial image restoration with local cosine-fitting energy

In practice, medical images such as MRI images and images of ultrasonoscopy always have the intensity inhomogeneity problem [30,31]. In this section, we will use image-updating method to combine the local information with the cosine-fitting energy [37]. We proposed the IRLCF model to process all kinds of original images, including images with intensity homogeneity and intensity inhomogeneity. Let I: $\Omega \to R$ be a given image and C be a closed curve. We use the local intensity characteristics and image-updating strategy to modify the data fidelity term. For a given point $p \in \Omega$ and consider any neighborhood q of point p within radius ρ, i.e. $N_p = \{q | |p - q| \leq \rho\}$. The given curve C divides the image domain Ω into two regions: Γ and $\Omega \backslash \Gamma$, where Γ represents the image domain inside C and $\Omega \backslash \Gamma$ represents the one outside C [32]. We define the IRLCF energy as follows:

$$\varepsilon^{IRLCF}(C, f_1(x), f_2(x)) = \lambda_1 \sum_{p \in \Gamma} \left\{ \sum_{q \in N_p} K(x_p - x_q)[-cos(f(x_q) - f_1(x_p))] \right\}$$
$$+ \lambda_2 \sum_{p \in \Omega \backslash \Gamma} \left\{ \sum_{q \in N_p} K(x_p - x_q)[-cos(f(x_q) - f_2(x_p))] \right\}, \quad (19)$$

where $f(x)$ is the updated image during the updating process. The specifics of the updating method will be introduced in detail in the next section. λ_1 and λ_2 are positive constants. $f(x_q)$, $f_1(x_p)$, and $f_2(x_p)$ are vectors. K is a nonnegative weighting function and when $q \notin N_p$ it satisfies $K(x_p - x_q) = 0$. x_p, x_q are the coordinates of points p, q, respectively. The weighting function K can be chosen as a different kernel function. In this study we choose the Gaussian kernel function as the weighting function [33]. Its specific form is expressed as follows:

$$K_\sigma(z) = \begin{cases} \dfrac{1}{a} e^{-|z|^2/2\sigma^2}, & |z| \leq \rho \\ 0, & else. \end{cases} \quad (20)$$

where a is a normalization constant, i.e. $\int_{|z| \leq \rho} K_\sigma(z)dz = 1$, and σ is the standard deviation. Meanwhile the image intensity of a local regional center in the fixed point p can be approximate to f_1 and f_2 that correspond to the inside and outside regions of the curve. Every fixed point can be controlled by the parameter σ.

As for a gray image with pixel values between [0, 1], when the object of the curve C and background do not match, this energy is negative in the interval (0, 1]. The initial value of the level set function outside the curve C is -1 and that inside the curve C is $+1$. Minimizing ε^{IRLCF} allows the curve to detect objects of interest in the gray image. In short, this cosine-fitting energy can get the similar effect of the fitting energy of the LBF model, but its cosine-power error within [0, 1] is smaller than the square error. In other words, the cosine-fitting energy is less sensitive to noise than the LBF model.

In order to deal with the change of topological structure, we rewrite the IRLCF level set function as an energy functional. The curve C is expressed as a zero-level set of function ϕ. $\Omega \to R$, $\phi > 0$ is for the inside of the contour C and $\phi < 0$ is for the outside of C. Considering the penalty term of the contour length, we can rewrite the energy functional in the following form:

$$\varepsilon(C, f_1(x), f_2(x)) = \lambda_1 \sum_{p \in \Gamma} \left\{ \sum_{q \in N_p} K(x_p - x_q)[-cos(f(x_q) - f_1(x_p))] \right\}$$
$$+ \lambda_2 \sum_{p \in \Omega \backslash \Gamma} \left\{ \sum_{q \in N_p} K(x_p - x_q)[-cos(f(x_q) - f_2(x_p))] \right\}$$
$$+ \mu \sum_{x \in \Omega} \delta(\phi)|\nabla \phi|, \quad (21)$$

In order to gain accurate results and a stable level set estimation [29], we introduce a level set regularization term and express it in the following energy functional:

$$P(\phi) = \frac{1}{2} \sum_{x \in \Omega} (|\nabla \phi| - 1)^2, \quad (22)$$

Combining the energy functional of Eq. (21) and regularization term of Eq. (22), we can obtain the energy functional as follows:

$$J = \varepsilon(\phi, f_1, f_2) + \nu P(\phi), \quad (23)$$

The total energy functional of an image in domain Ω can be defined directly as the following form:

$$J(\phi, f_1, f_2) = \sum_{j=1}^{2} \lambda_j \sum_{p \in \Omega} \left\{ \sum_{q \in N_p} K(x_p - x_q) \left[-\cos\left(f(x_q) - f_j(x_p)\right) \right] \right\} M_j(\phi(x_q))$$
$$+ \mu \sum_{x \in \Omega} \delta(\phi) |\nabla \phi| + \nu \sum_{x \in \Omega} \frac{1}{2} (|\nabla \phi| - 1)^2, \tag{24}$$

where $M_1 = H(\phi)$ and $M_2 = 1 - H(\phi)$. $H(z)$ is the Heaviside function. $\delta(z)$ is the δ-Dirac function. They are defined as follows, respectively:

$$H(z) = \begin{cases} 1, & if \ z \geq 0 \\ 0, & if \ z < 0 \end{cases} \tag{25}$$

and

$$\delta(z) = \frac{d}{dz} H(z), \tag{26}$$

In practice, the Heaviside function and δ-Dirac function can be approximated by smooth functions H_ε and δ_ε accordingly, i.e.,

$$H_\varepsilon(z) = \frac{1}{2} \left[1 + \frac{2}{\pi} \arctan\left(\frac{z}{\varepsilon}\right) \right], \tag{27}$$

and

$$\delta_\varepsilon(z) = \frac{1}{\pi} \frac{\varepsilon}{\varepsilon^2 + z^2}, \tag{28}$$

Therefore, the total energy functional takes the following form:

$$J(\phi, f_1, f_2) = \lambda_1 \sum_{p \in \Omega} \left\{ \sum_{q \in N_p} K(x_p - x_q) [-\cos(f(x_q) - f_1(x_p))] H_\varepsilon(\phi) \right\}$$
$$+ \lambda_2 \sum_{p \in \Omega} \left\{ \sum_{q \in N_p} K(x_p - x_q) [-\cos(f(x_q) - f_2(x_p))](1 - H_\varepsilon(\phi)) \right\} \tag{29}$$
$$+ \mu \sum_{x \in \Omega} \delta_\varepsilon(\phi) |\nabla \phi| + \nu \sum_{x \in \Omega} \frac{1}{2} (|\nabla \phi| - 1)^2,$$

3.3. The recovery method of the updated image

Most of the medical images, especially MRI images, have more or less Gaussian noise [38]. Due to the requirements of its characteristics and integrity of medical information, we cannot recover the medical images directly. In this study we recover the images corresponding to the points of the level set curves and drive the level set curves close to the objects of interest. Then we superimpose the level set curve over the original medical images to optimize the selection of objects of interest.

The regularization method is the frequently-used method to improve the quality of recovered images. In this study we use the total variation superinfection group regularization method to recover images [19]. This method performs preferably in images with the Gaussian noise. We verify its superiority by comparing it with other methods in numerical experiments.

Let us consider a classical noise interference model

$$g = f + \eta, \tag{30}$$

where the image with noise is represented by g. f is the image without noise, η is the Gaussian noise with zero-mean.

Image recovery is a kind of ill-posed problem. We can obtain the stable and accurate results through the regularization method [11]. We build the following recovery model:

$$\min_{f} \left\{ \frac{1}{2} \|g - f\|_2^2 + \lambda \varphi(f) \right\}, \tag{31}$$

where $\varphi(f)$ is a regularization term. Based on the idea of the overlapping set of space [39], we use the overlapping set of space of the two-dimensional image in the gradient domain to improve the function and to recover the image.

Let us select a $K \times K$ window with the center at (i, j) in image f, $f \in \mathbb{R}^{n \times n}$ for calculating the total variation of the overlapped region in f by the window:

$$\tilde{f}_{i,j,K} = \begin{bmatrix} f_{i-m_1,j-m_1} & f_{i-m_1,j-m_1+1} & \cdots & f_{i-m_1,j+m_2} \\ f_{i-m_1+1,j-m_1} & f_{i-m_1+1,j-m_1+1} & \cdots & f_{i-m_1+1,j+m_2} \\ \vdots & \vdots & \ddots & \vdots \\ f_{i+m_2,j-m_1} & f_{i+m_2,j-m_1+1} & \cdots & f_{i+m_2,j+m_2} \end{bmatrix} \in \mathbb{R}^{K \times K}, \tag{32}$$

where $m_1 = [\frac{K-1}{2}]$, $m_2 = [\frac{K}{2}]$, here $[x]$ represents the largest integer but less than x. Since image f can also be expressed as a vector that is obtained by stretching the corresponding $n \times n$ matrix, i.e. $f \in \mathbb{R}^{n^2}$, we can also pack K in $\tilde{f}_{i,j,K}$ as a vector $f_{i,j,K}$ according to the column. Accordingly, let $f_{i,j}$ represents the $[(n-1)j+i]$th element of the vector f, the overlapping group function can be defined as follows:

$$\phi(f) = \sum_{i,j=1}^{n} \left\| f_{i,j,K} \right\|_2 \tag{33}$$

We choose the regularization term $\varphi(f)$ as

$$\varphi(f) = \phi(D_x f) + \phi(D_y f), \tag{34}$$

where, $D_x, D_y \in \mathbb{R}^{n^2 \times n^2}$ are first-order difference matrices. As the image is sparse in the gradient domain, we refer the function $\varphi(f)$ as the total variation with overlapping group sparsity (OGS-TV) regular function. So on the basis of the OGS-TV regular function in the Eq. (33), we propose the following recovery model:

$$\min_f \left\{ \frac{1}{2}\|g - f\|_2^2 + \lambda(\phi(D_x f) + \phi(D_y f)) \right\}, \tag{35}$$

where, $\lambda > 0$ is the regularization parameter.

Because the pixel values of digital images are finite, the pixel values are limited to some domain, such as $[a_l, a_u]$. This kind of limitation is called box constraints. All images considered in this study are 8-bit gray images. In other words, pixel values are in the dynamic range of [0, 255]. We impose the box constraint ($\Omega = [0, 255]$) to the restored images. Similar work can be found in [5]. The indicator function of a gather is defined as:

$$\mathbb{I}_\Omega = \begin{cases} 0, & x \in \Omega \\ +\infty, & x \notin \Omega \end{cases} \tag{36}$$

Combined with the indicator function defined in Eq. (36), the minimization problem Eq. (35) is turned into the following equivalent:

$$\min_{f,v_1,v_2,z} \left\{ \frac{1}{2}\|g - f\|_2^2 + \lambda(\phi(v_1) + \phi(v_2)) + \mathbb{I}_\Omega(z) \right\}, \tag{37}$$
$$\text{s.t.} \quad D_x f = v_1, D_y f = v_2, f = z,$$

The expanded Lagrange function [23] corresponding to Eq. (37) is:

$$\mathcal{L} = \frac{1}{2}\|g - f\|_2^2 + \lambda(\phi(v_1) + \phi(v_2)) + \mathbb{I}_\Omega(z)$$
$$+ \frac{\delta}{2}\left\{ \left\| D_x f - v_1^k + p_1^k \right\|_2^2 + \left\| D_y f - v_2^k + p_2^k \right\|_2^2 + \left\| f - z^k + p_3^k \right\|_2^2 \right\} \tag{38}$$

where p_1^k, p_2^k and p_3^k are the Lagrangian multipliers. On the basis of the well-known ADMM frame [7], we can obtain the iterative scheme for solving Eq. (37).

$$f^{k+1} = \arg\min_f \frac{1}{2}\|g - Hf\|_2^2$$
$$+ \frac{\delta}{2}\left\{ \left\| D_x f - v_1^k + p_1^k \right\|_2^2 + \left\| D_y f - v_2^k + p_2^k \right\|_2^2 + \left\| f - z^k + p_3^k \right\|_2^2 \right\}, \tag{39}$$

$$\begin{pmatrix} v_1^{k+1} \\ v_2^{k+1} \\ z^{k+1} \end{pmatrix} = \arg\min_{v_1,v_2,z} \frac{\delta}{2}\left\{ \left\| D_x f^{k+1} - v_1 + p_1^k \right\|_2^2 + \left\| D_y f^{k+1} - v_2 + p_2^k \right\|_2^2 + \left\| f^{k+1} - z + p_3^k \right\|_2^2 \right\}$$
$$+ \lambda(\phi(v_1) + \phi(v_2)) + \mathbb{I}_\Omega(z), \tag{40}$$

$$\begin{pmatrix} p_1^{k+1} \\ p_2^{k+1} \\ p_3^{k+1} \end{pmatrix} = \begin{pmatrix} p_1^k + \left(D_x f^{k+1} - v_1^{k+1}\right) \\ p_2^k + \left(D_y f^{k+1} - v_2^{k+1}\right) \\ p_3^k + \left(f^{k+1} - z^{k+1}\right) \end{pmatrix}, \tag{41}$$

Now, let us solve the relevant subproblems. The minimizing problem Eq. (39) of the variate f is a least-square problem, which can also be formulated in the following form:

$$
\begin{aligned}
&(H^T H + \delta D_x{}^T D_x + \delta D_y{}^T D_y + \delta I) f^{k+1} \\
&= H^T g + \delta \left(D_x{}^T (v_1^k - p_1^k) + D_y{}^T (v_2^k - p_2^k) + z^k - p_3^k \right)
\end{aligned}
\tag{42}
$$

Because the parameter δ is positive, the matrix on the left side of Eq. (42) is invertible. Under the periodic boundary condition, the matrices H, D_x and D_y are block circulant and circulant block matrix (BCCB) [19]. The advantage of this matrix is that it can be diagonalized by a fast-Fourier transformation. To be more specific, suppose $\wedge_H$, $\wedge_{D_x}$, $\wedge_{D_y}$ are the spectra of matrices H, D_x and D_y, respectively, equation Eq. (42) can then be rewritten as

$$
\begin{aligned}
&F^* \; (\wedge_H^* \wedge_H + \delta \wedge_{D_x}^* \wedge_{D_x} + \delta \wedge_{D_y}^* \wedge_{D_y} + \delta I) F f^{k+1} \\
&= F^* (\wedge_H^* Fg + \delta \wedge_{D_x}^* F(v_1^k - p_1^k) + \delta \wedge_{D_y}^* F(v_2^k - p_2^k) + F(z^k - p_3^k))
\end{aligned}
\tag{43}
$$

where F is the discrete Fourier transform and $*$ denotes conjugate transpose. We can obtain f^{k+1} as follows:

$$
\begin{aligned}
f^{k+1} = F^*[(\wedge_H^* \wedge_H + \delta \wedge_{D_x}^* \wedge_{D_x} + \delta \wedge_{D_y}^* \wedge_{D_y} + \delta I)^{-1} (\wedge_H^* Fg + \delta \wedge_{D_x}^* F(v_1^k - p_1^k) \\
+ \delta \wedge_{D_y}^* F(v_2^k - p_2^k) + F(z^k - p_3^k))]
\end{aligned}
\tag{44}
$$

Apparently, the subproblems of finding v_1, v_2, z are decoupled. That is to say, they can be solved separately. For v_1 we have:

$$
v_1^{k+1} = \arg \min_{v_1} \frac{\delta}{2} \left\| v_1 - \left(D_x f^{k+1} + p_1^k \right) \right\|_2^2 + \lambda \phi(v_1)
\tag{45}
$$

Similarly, v_2 can be obtained as

$$
v_2^{k+1} = \arg \min_{v_2} \frac{\delta}{2} \left\| v_2 - \left(D_y f^{k+1} + p_2^k \right) \right\|_2^2 + \lambda \phi(v_2)
\tag{46}
$$

For the subproblem of z, it can be solved as

$$
z^{k+1} = \arg \min_z \left\{ \frac{1}{2} \left\| f^{k+1} + p_3^k - z \right\| + \mathbb{I}_\Omega(z) \right\}
\tag{47}
$$

Based on the above discussion, we can solve Eq. (35) by the Algorithm 1 as shown below:

Algorithm 1 Based on the OGS-TV recovery algorithm for solving Eq. (35).

---

1. Initialization: initial point, maximum iterations N, $r, t = 1, 2, \cdots, n$;
2. Iteration: $v_1^k = v_2^k = g$, $k = 0$, $\beta > 0$, $\delta > 0$, N, K, $p_i^k = \mathbf{0}$
   (1) Calculate f^{k+1}: obtained by solving Eq. (44);
   (2) Calculate v_1^{k+1}: obtained by solving Eq. (45);
   (3) Calculate v_2^{k+1}: obtained by solving Eq. (46);
   (4) Calculate z^{k+1}: obtained by solving Eq. (47);
   (5) Update p_i^{k+1}, $i = 1, 2, 3$: obtained by solving Eq. (41);
   (6) $k = k + 1$;
   (7) Going back to step (1) until the stop condition is met.

Obviously, Algorithm 1 meets the ADMM frame. If the steps from the first to the fourth can be calculated accurately, all subproblems have closed solutions and Algorithm 1 is convergent. Because the subproblems in the second and third steps are solved by the majorization-minimization (MM) iteration [9], it failed to obtain the accurate solution. Only if their errors of the solutions are additive, can the Algorithm 1 be convergent.

3.4. The solving method of the IRLCF model and computational process

In this section, we mainly focus on the solution of the IRLCF-based image segmentation problem. We propose a new minimization method to solve the energy functional Eq. (29) and rewrite the energy functional model under the discrete conditions. To minimize alternatively the energy ϕ and f_j, we fix two groups of variables and solve another one alternatively [36].

1) Firstly, fix ϕ and minimize energy function H_ε with respect to the functions $f_1(x)$ and $f_2(x)$. Then we can obtain a formula as follows:

$$
\begin{aligned}
\min_{f_1, f_2} G(\phi, f_1(x), f_2(x)) = \lambda_1 \sum_{p \in \Omega} \left\{ \sum_{q \in N_p} K(x_p - x_q)[-\cos(f(x_q) - f_1(x_p))]H_\varepsilon(\phi) \right\} \\
+ \lambda_2 \sum_{p \in \Omega} \left\{ \sum_{q \in N_p} K(x_p - x_q)[-\cos(f(x_q) - f_2(x_p))](1 - H_\varepsilon(\phi)) \right\}.
\end{aligned}
\tag{48}
$$

We can solve for functions $f_1(x)$ and $f_2(x)$ through the Euler-Lagrange function [10,27] in Eq. (48):

$$
f_j(x_p) = \arctan \frac{\sum_{q \in N_p} K(x_p - x_q)\left[M_j^\varepsilon(\phi) \sin f(x_p)\right]}{\sum_{q \in N_p} K(x_p - x_q)\left[M_j^\varepsilon(\phi) \cos f(x_p)\right]}, j = 1, 2
\tag{49}
$$

or

$$
f_j(x_p) = \arctan \frac{K(x_p) * \left[M_j^\varepsilon(\phi) \sin f(x_p)\right]}{K(x_p) * \left[M_j^\varepsilon(\phi) \cos f(x_p)\right]}, j = 1, 2
\tag{50}
$$

where $M_1^\varepsilon(\phi) = H_\varepsilon(\phi)$, and $M_2^\varepsilon(\phi) = 1 - H_\varepsilon(\phi)$, $f(x)$ can be obtained by the above section.

2) Then, as to the energy functional in Eq. (29) with respect to the minimized ϕ of the fix functions $f_1(x)$ and $f_2(x)$, the gradient-descent formula that is correspondent to the Euler–Lagrange function can be obtained as is shown in formula (51)

$$
\begin{aligned}
\frac{\partial \phi}{\partial t} = & -\delta_\varepsilon(\lambda_1 e_1 - \lambda_2 e_2) - \mu \delta_\varepsilon \left(\partial_x^* \frac{w}{\sqrt{w^2 + v^2}} + \partial_y^* \frac{v}{\sqrt{w^2 + v^2}} \right) \\
& + v \left(\Delta \phi + \left(\partial_x^* \frac{w}{\sqrt{w^2 + v^2}} + \partial_y^* \frac{v}{\sqrt{w^2 + v^2}} \right) \right)
\end{aligned}
\tag{51}
$$

where, $w = \partial_x \phi$, $v = \partial_y \phi$ and δ_ε are given by Eq. (28) and e_1, e_2 are defined as follows:

$$
e_j(x) = \sum_{q \in N_p} K(x_p - x_q)(-\cos(f(x_q) - f_j(x_p))), \ j = 1, 2
\tag{52}
$$

The evolved level set function ϕ can be obtained by iterating Eq. (51).

Based on the above discussion, we developed an algorithm for solving Eq. (48), denoted by Algorithm 2 shown as below.

Algorithm 2 A IRLCF-based recovery algorithm for solving Eq. (48).

---

1. Initialization: inputting the original image $I_0(x)$, given the initial level set ϕ, utilizing Eq. (49) to get $f_1(x)$ and $f_2(x)$, given the level set maximum iterations N;
2. Iteration: setting the step size Δt, substituting it into Eq. (51) and using the iteration method to obtain the evolved ϕ;
3. Updating the image: getting the coordinate point of the evolved level set curve ϕ, using Eq. (37) to recover the image $f(x)$;
4. Substituting the recovered image $f(x)$ into Eq. (49), and repeating the iteration process;
5. Stopping condition: when the maximum number of iterations is reached, the level set curve evolution stops.

In the level set evolution of the Eq. (48), the first term can be obtained by the local cosine-fitting energy. It plays a leading role in segmenting an image with intensity inhomogeneity. The next two terms are the regular terms. They are used to keep the regularity of the contour and the level set function.

3.5. The IRLCF model analysis

Compared with the LBF and CVMST models, an essential difference is that the L0MS model uses the real-time updating strategy. When an image is noiseless piecewise-constant image, the result is absolutely accurate. However, in most cases the image has more or less noises. Under such a circumstance, we try to develop an algorithm that is more anti-noise. The level set segmentation algorithm can remove the noise points in the level set curve and intensify the boundary information to obtain a smoother and more truthful contour C of the object of interest. Therefore, we can demonstrate that the IRLCF model is not as sensitive to noise as the LBF, CVMST, and L0MS models. Similarly, the IRLCF model can be considered as a local application that centers at every pixel of the level set curve ϕ. It also makes the IRLCF model more robust.
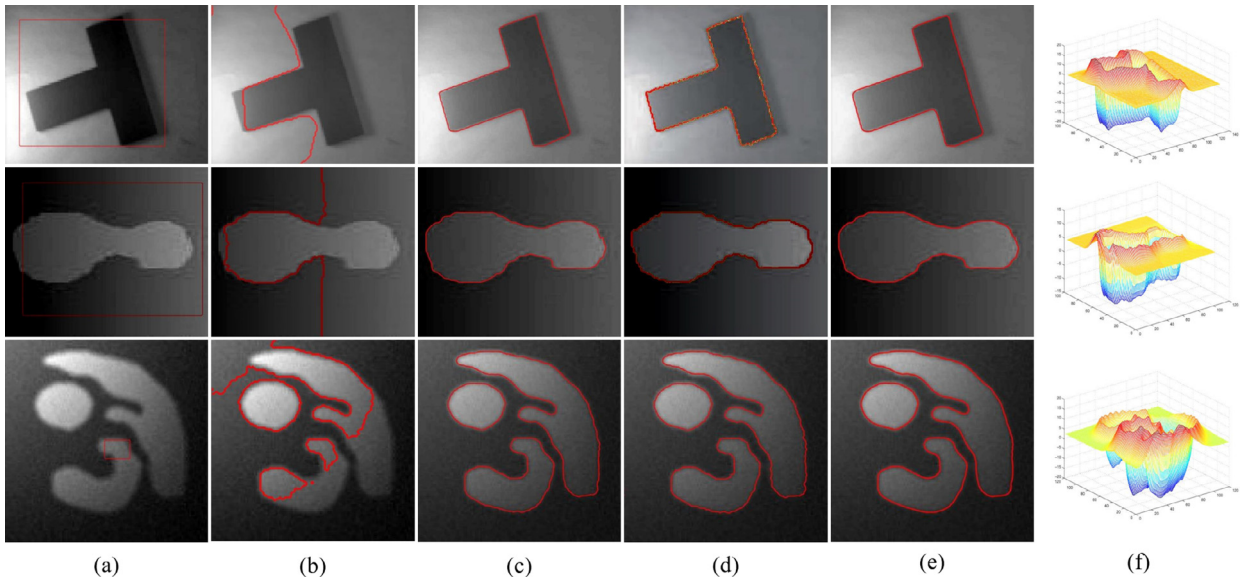
Fig. 1. Segmentation results of various models of synthetic images. (a) (Column 1): input images with initial contours; (b) (Column 2): The segmentation results of the CVMST model; (c) (Column 3): The segmentation results of the LBF model; (d) (Column 4): The segmentation results of the L0MS model; (e) (Column 5): The segmentation results of the IRLCF model; and (f) (Column 6): The evolved level set function image of Column 5.

4. Experimental results and discussion

In this section, we will test and discuss the performance of the IRLCF model and the applications of the model to different types of images. Unless otherwise specified, we set the default parameters as $\varepsilon = 1.0$ and $\Delta t = 0.4$ in the IRLCF model. In order to prevent an image from being over recovered, we will use the strategy that updates the image periodically. For recovering an image, we chose the window size as 3×3, i.e. $K = 3$.

4.1. Segmentation results on standard images by the IRLCF model

We tested the IRLCF model on an image with blurred boundaries and intensity inhomogeneity. We set $\lambda_1 = 255 \times 8$, $\lambda_2 = 255 \times 7.99$, $\mu = 9$, $\Delta t = 0.9$ for the first image (top in the first column of Fig. 1), $\lambda_1 = 255 \times 5$, $\lambda_2 = 255 \times 5$, $\mu = 7$, $\Delta t = 0.9$ for the second image (second from the top in the first column of Fig. 1), $\lambda_1 = 255 \times 8$, $\lambda_2 = 255 \times 8.003$, $\mu = 10$, $\Delta t = 0.5$ for the third image (bottom of the first column of Fig. 1). Fig. 1 shows the results from the CVMST, L0MS, LBF and IRLCF models.

Fig. 1 shows the segmentation results of synthetic images with intensity inhomogeneity. From Fig. 1(b), we can see that the segmentation results of the CVMST model are inferior to the results by the other models. The model did not successfully segment the objects. Fig. 1(c) and (e) are the segmentation results of the IRLCF model and the LBF model, respectively. We can see that these two models are quite efficient and the boundaries are smooth. Fig. 1(d) shows the segmentation results of the L0MS model. We can see that the edges of the target objects located by this model are pretty accurate. However, due to the influence of the L_0 norm, the edges of the segmented images were intensively sharpened. Some of the segmentation results do not meet virtual requirements of the edges. Fig. 1(f) shows the segmented level set function image of the IRLCF model. From the results we can see that the IRLCF model can make edges smoother than other models and the level set function is more disciplinary, showing the advantage of the cosine-fitting method in smoothing edges of segmented objects.

We also tested the IRLCF model on images with noise and intensity inhomogeneity. Here are the values of parameters we set: $\lambda_1 = 255 \times 5$, $\lambda_2 = 255 \times 5.01$, $\mu = 15$, $\Delta t = 0.9$ for the first image (top in the first column of Fig. 2); $\lambda_1 = 255 \times 8$, $\lambda_2 = 255 \times 8$, $\mu = 10$, $\Delta t = 0.4$ for the second image(second from the top in the first column of Fig. 2); $\lambda_1 = 255 \times 8$, $\lambda_2 = 255 \times 8.003$, $\mu = 10$, $\Delta t = 0.5$ for the third image (third from the top in the first column of Fig. 2); $\lambda_1 = 255 \times 8$, $\lambda_2 = 255 \times 8$, $\mu = 33.7$, $\Delta t = 0.7$ for the fourth image(fourth from the top in the first column of Fig. 2); $\lambda_1 = 255 \times 8$, $\lambda_2 = 255 \times 8$, $\mu = 36$, $\Delta t = 0.8$ for the last image in the first column in Fig. 2. Fig. 2 shows the segmentation results from the CVMST, L0MS, LBF, and IRLCF models.

Fig. 2 shows the segmentation results by the CVMST, L0MS, LBF, and IRLCF algorithms on images with noise and intensity inhomogeneity. Fig. 2(a) shows the initial level set contours of images with different noise levels and intensity inhomogeneity. Fig. 2(b) shows the segmentation results of the CVMST model from which we can see that it did not accurately segment the gray images with noise and intensity inhomogeneity, but it performed well for noise images with uniform intensity. Comparing to the IRLCF model, the locating accuracy of the CVMST model is worse. Fig. 2(c) shows the segmentation results
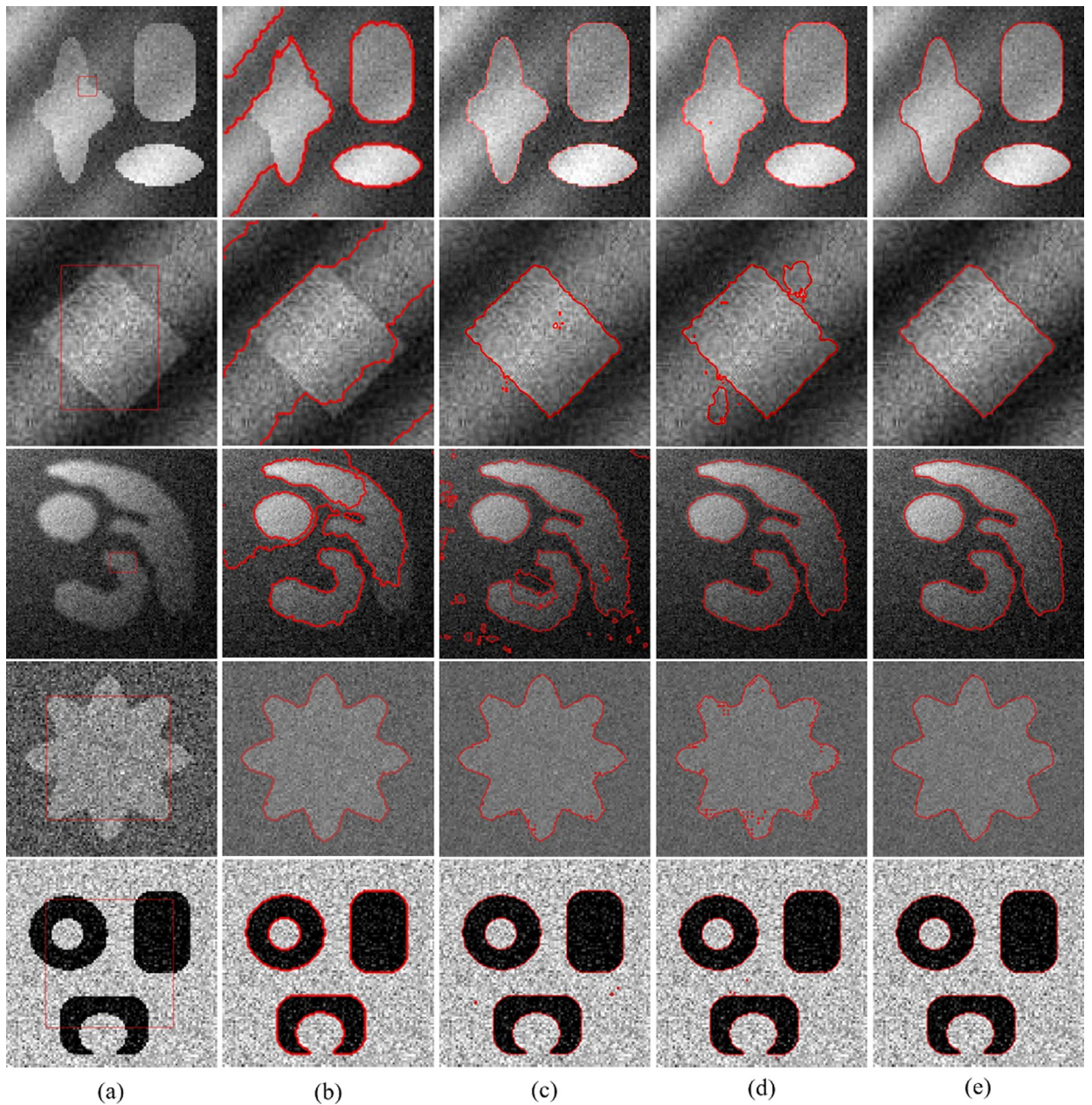
Fig. 2. Segmentation results of various models on synthetic images with noise and intensity inhomogeneity. (a) (Column 1): Input images with initial level set contours; (b) (Column 2): The segmentation results of the CVMST model; (c) (Column 3): The segmentation results of the LBF model; (d) (Column 4): The segmentation results of the L0MS model; (e) (Column 5): The segmentation results of the IRLCF model.

of the LBF model from which we can see the locating accuracy of the LBF model is better than the CVMST model, but its segmentation accuracy is poorer, and the segmented edges are rough, which makes the results less than satisfactory. From Fig. 2(d) we can see that the L0MS model performed poorly in segmenting noise images, resulting in more incorrect and insufficient segmentation situations. This may indicate that the immunity of this algorithm to noise is unsatisfactory. From Fig. 2(e) we can see that the new method developed in this study extracted objects successfully from the five images. It can be observed that the proposed IRLCF model is more efficient and robust than the CVMST, L0MS and LBF models, especially for images with both noise and intensity inhomogeneity (see the second row from the top in Fig. 2).

We also tested the IRLCF model on standard medical images. The values of parameters that we set are: λ_1=255 × 5, λ_2=255 × 5, $\mu = 7$, $\Delta t = 0.9$ for the first image(top in the first column of Fig. 3); $\lambda_1 = 255 \times 8$, $\lambda_2 = 255 \times 8.01$, $\mu = 10$, $\Delta t = 1.2$ for the second image (second from the top in the first column of Fig. 3); $\lambda_1 = 255$, $\lambda_2 = 255$, $\mu = 2.8$, $\Delta t = 1$
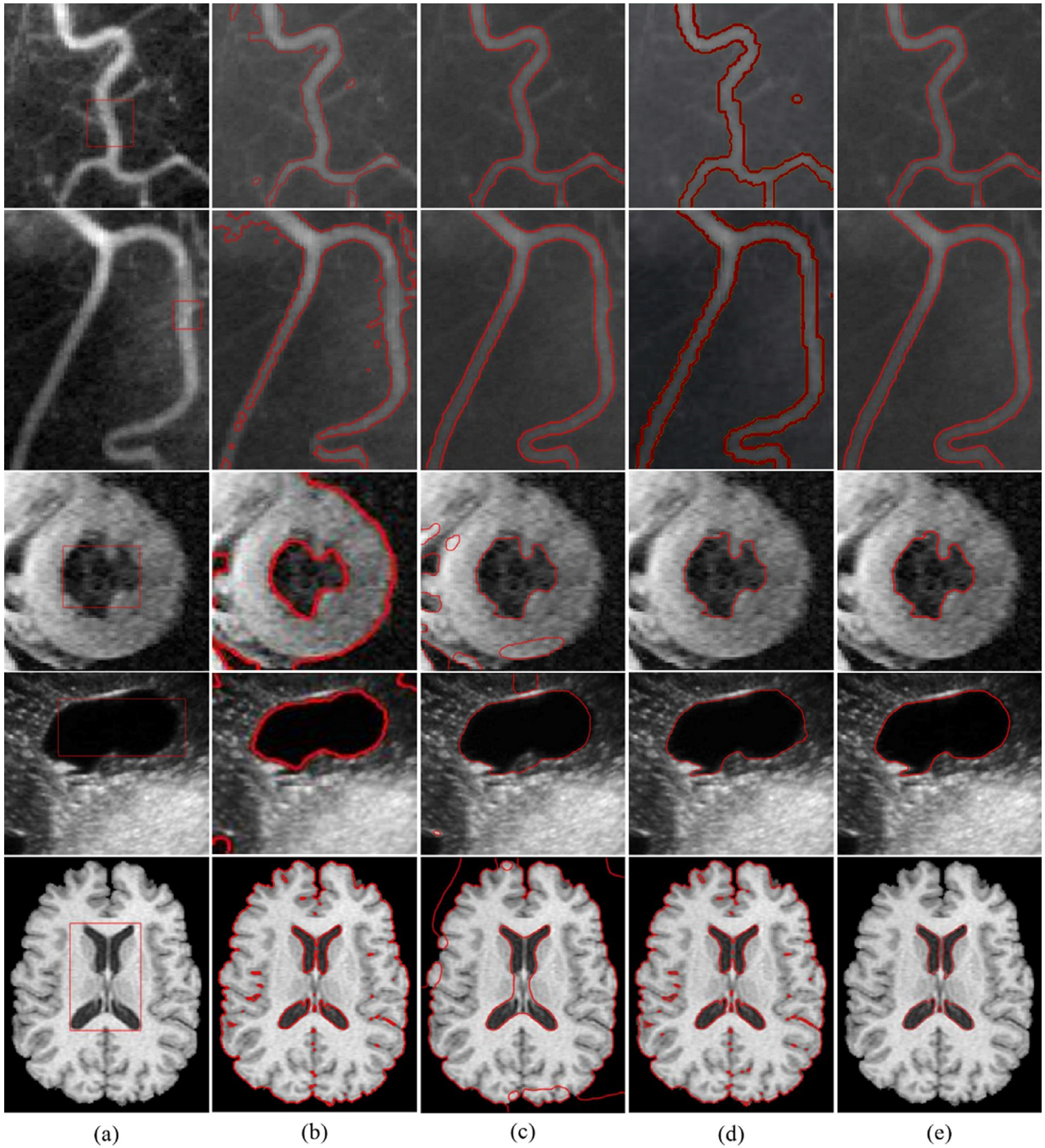
Fig. 3. Segmentation results from various models on standard medical images. (a) (Column 1): Input images with initial level set contours; (b) (Column 2): The segmentation results of the CVMST model; (c) (Column 3): The segmentation results of the LBF model; (d) (Column 4): The segmentation results of the L0MS model; and (e) (Column 5): The segmentation results of the IRLCF model.

for the third image (third from the top in the first column of Fig. 3); λ_1 = 255 × 4, λ_2 = 255 × 4, $\mu = 23$, $\Delta t = 0.8$ for the fourth image (fourth from the top in the first column of Fig. 3); λ_1 = 255 × 8.037, λ_2 = 255 × 8, $\mu = 21$, $\Delta t = 0.25$ for the last image in Fig. 3 (bottom in the first column of Fig. 3). Fig. 3 shows the segmentation results from the CVMST, L0MS, LBF, and IRLCF models.

Fig. 3 shows the segmentation results on standard medical images using the CVMST, L0MS, LBF, and IRLCF models. Fig. 3(a) is the input images with initial contours and Fig. 3(b) is the segmentation results of the CVMST model. We can see that the CVMST model has poor performance in segmenting blood vascular images. However, it can obtain more ac-

Table 1

CPU time (in seconds) comparison among the LBF, CVMST, DRLSE, and IRLCF algorithms.

Image	Resolution	IRLCF		LBF		CVMST		DRLSE	
		iterations	CPU time	iterations	CPU time	iterations	CPU time	iterations	CPU time
T intersection	127×96	45	2.644	300	4.676	1138	4.495	210	2.659
Three graphics	120×119	403	5.107	240	3.348	1067	3.581	310	4.770
NonUniform	79×75	100	2.315	200	2.916	688	2.016	210	3.116
Noisystar	98×90	152	4.287	400	5.638	904	2.378	1010	4.701
Noiseimage	101×99	47	2.197	240	3.683	632	2.435	810	4.025
Vessel1	111×110	72	3.35	150	2.636	905	3.688	210	3.562
Vessel2	103×131	67	3.596	220	3.668	1088	5.157	190	3.300
Ultrasound	147×131	85	2.854	300	5.030	1002	4.441	310	5.138
MRIhead	200×250	71	4.778	1100	16.800	986	7.351	510	5.950

Table 2

Changes in segmentation accuracies (SAR, OSR, and USR) of the IRLCF model with increasing noise levels in the Heptagon, Horse, and 3D images.

Images	Variance	Heptagon			Horse			3D		
		SAR	OSR	USR	SAR	OSR	USR	SAR	OSR	USR
Gaussian white noise	0.02	99.950%	0.013%	0.026%	99.954%	0.023%	0.023%	99.849%	0.000%	0.151%
	0.1	99.943%	0.024%	0.033%	99.865%	0.030%	0.105%	99.734%	0.099%	0.167%
	0.2	99.937%	0.027%	0.036%	99.826%	0.045%	0.128%	99.734%	0.214%	0.052%
	0.3	99.933%	0.038%	0.029%	99.880%	0.030%	0.090%	99.510%	0.427%	0.063%
	0.5	99.868%	0.132%	0.000%	99.925%	0.053%	0.023%	98.316%	1.668%	0.016%
Random noise	Rate	SAR	OSR	USR	SAR	OSR	USR	SAR	OSR	USR
	0.2	99.980%	0.007%	0.013%	99.857%	0.045%	0.098%	99.562%	0.115%	0.323%
	0.3	99.931%	0.017%	0.052%	99.281%	0.165%	0.555%	99.395%	0.120%	0.485%
	0.4	99.852%	0.034%	0.113%	99.077%	0.068%	0.855%	99.187%	0.109%	0.704%
	0.6	99.315%	0.185%	0.500%	96.992%	0.090%	2.918%	98.019%	0.438%	1.543%
	0.8	98.426%	0.006%	1.568%	94.884%	0.083%	5.033%	96.685%	0.427%	2.888%

curate results in segmenting ultrasound and brain MRI images, but there are still errors in image segmentation. Fig. 3(c) shows the segmentation results of the LBF model. We find it can obtain very accurate results in segmenting blood vascular images, but it fails to segment other medical images. Fig. 3(d) shows the segmentation results of the L0MS model. Objects can be accurately located but they are affected by edge sharpening, while for medical images, the edges of the segmented images should be smooth. The L0MS model also has errors in image segmentation. Compared with the other models, the IRLCF model has better performance in segmentation of different types of medical images.

4.2. CPU time compare

A Dell server with Intel(R) Xeon(R) CPU E5-2620 2∗2.00 GHz (2 processors) and 32GB RAM was used for simulation. The LBF, CVMST, and DRLSE algorithms were compared with the newly developed IRLCF algorithm in the CPU time in the segmentation of nine standard images, which include the first (T intersection) and the third (Three graphics) ones in Fig. 1, the first (NonUniform), the fourth (Noisy star) and the fifth (Noise image) ones in Fig. 2, and the first (Vessel 1), the second (Vessel 2), the fourth (Ultrasound) and the fifth (brain MRI) ones in Fig. 3. Table 1 shows the number of iterations and CPU time spent that is the average of 10 runs in segmentation of each image.

The CPU time shown in Table 1 indicates that for most images tested, the newly developed IRLCF algorithm costed similar or less amount of CPU time than the other three algorithms.

4.3. Analysis of robustness and noise immunity of the IRLCF algorithm

The robustness and noise immunity of the IRLCF algorithm are verified by applying it to different synthetic noisy images. The noise contained in the images is either the Gaussian white noise or random noise. Some synthetic images for test contain the Gaussian white noise with a variance of 0.02, 0.1, 0.2, 0.3, and 0.5, respectively. The other images contain the random noise of standard deviation of 20, 30, 40, 60, and 80, respectively. The peak signal to noise ratio (PSNR) value of images with the Gaussian white noise or random noise is calculated. The IRLCF algorithm, distance regularized level set evolution (DRLSE) [18] algorithms, and the level set evolution and algorithm bias field estimation (LSEBFE) [15] algorithms are compared for different types of input images and subsequent segmentation using the IRLCF, DRLSE, and LSEBFE algorithms. The parameter values we set are: λ_1=255 × 4, λ_2=255 × 4, $\mu = 10$, $\Delta t = 0.2$ in Figs. 4–6. Figs. 4–6 show the segmentation results of synthetic heptagon images, synthetic horse images, and synthetic 3D images with various levels of either Gaussian white noise or random noise. Simulation results show that the IRLCF algorithm has a robust noise immunity.
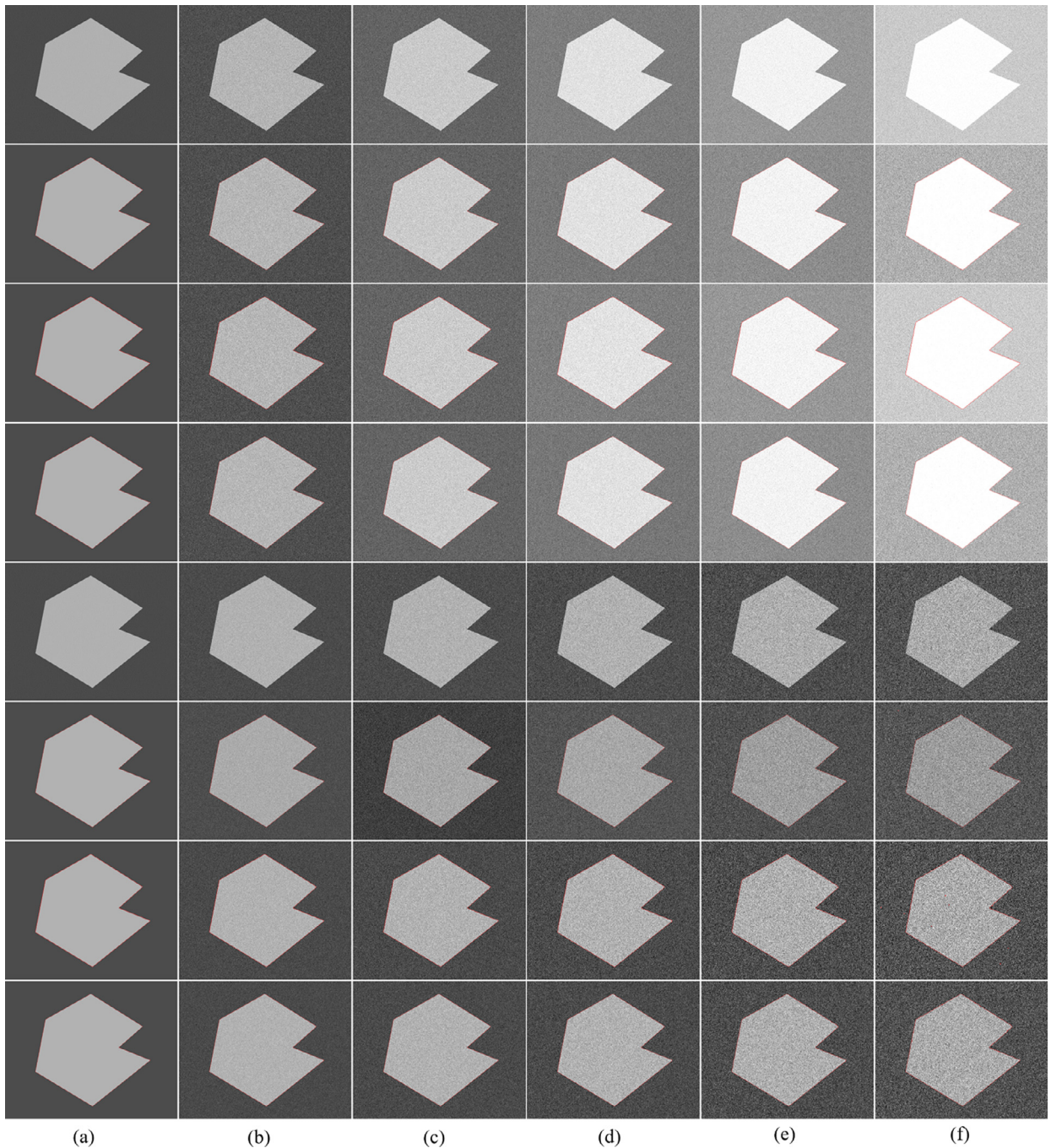
Fig. 4. Segmentation results of synthetic heptagon images that are contaminated by the Gaussian white noise or random noise. The first row from the top: synthesis heptagon images (from left to right) contaminated by the Gaussian white noise with a variance of 0.02, 0.1, 0.2, 0.3, and 0.5, respectively; and the PSNR values are 27.87, 25.51, 24.32, 24.09, and 24.07, respectively. The second to the fourth rows: segmentation results using the IRLCF, DRLSE, and LSEBFE algorithms. The fifth row: synthetic heptagon images (from the left to the right) contaminated by random noise of standard deviation of 20, 30, 40, 60, and 80, respectively; and the PSNR values are 22.11, 18.59, 16.08, 12.56, and 10.06, respectively. The sixth to the eighth rows: segmentation results using the IRLCF, DRLSE, and LSEBFE algorithms.

Fig. 5. Segmentation results of synthetic horse images that are contaminated by the Gaussian white noise or random noise. The first row from the top: synthetic horse images (from the left to the right) contaminated by the Gaussian white noise with a variance of 0.02, 0.1, 0.2, 0.3, and 0.5, respectively, and the PSNR values are 28.01, 25.59, 24.41, 24.17, 24.15, respectively. From the second to the fourth rows from the top: segmentation results using the IRLCF, DRLSE, and LSEBFE algorithms respectively. The fifth row: synthetic horse images contaminated by random noise of standard deviation of 20, 30, 40, 60, and 80, respectively, and the PSNR values were 22.10, 18.59, 16.03, 12.58, and 10.08, respectively. The sixth to the eighth rows: the segmentation results using the IRLCF, DRLSE, and LSEBFE algorithms.

The IRLCF algorithm has been used to perform image segmentation, and accuracy of segmentation is evaluated. Since the human eye is subjective in evaluating segmentation accuracy, we resort to quantitative methods for evaluation. Many methods have been developed for objective and quantitative evaluation of segmentation such as segmentation curve and coincidence rate of segmentation, etc. But these methods are not applicable for segmentation algorithms of the level set. Segmentation results are thus evaluated based on synthetic noisy images and the evaluation indices such as segmentation accuracy rate, over-segmentation rate, and under-segmentation rate [25].
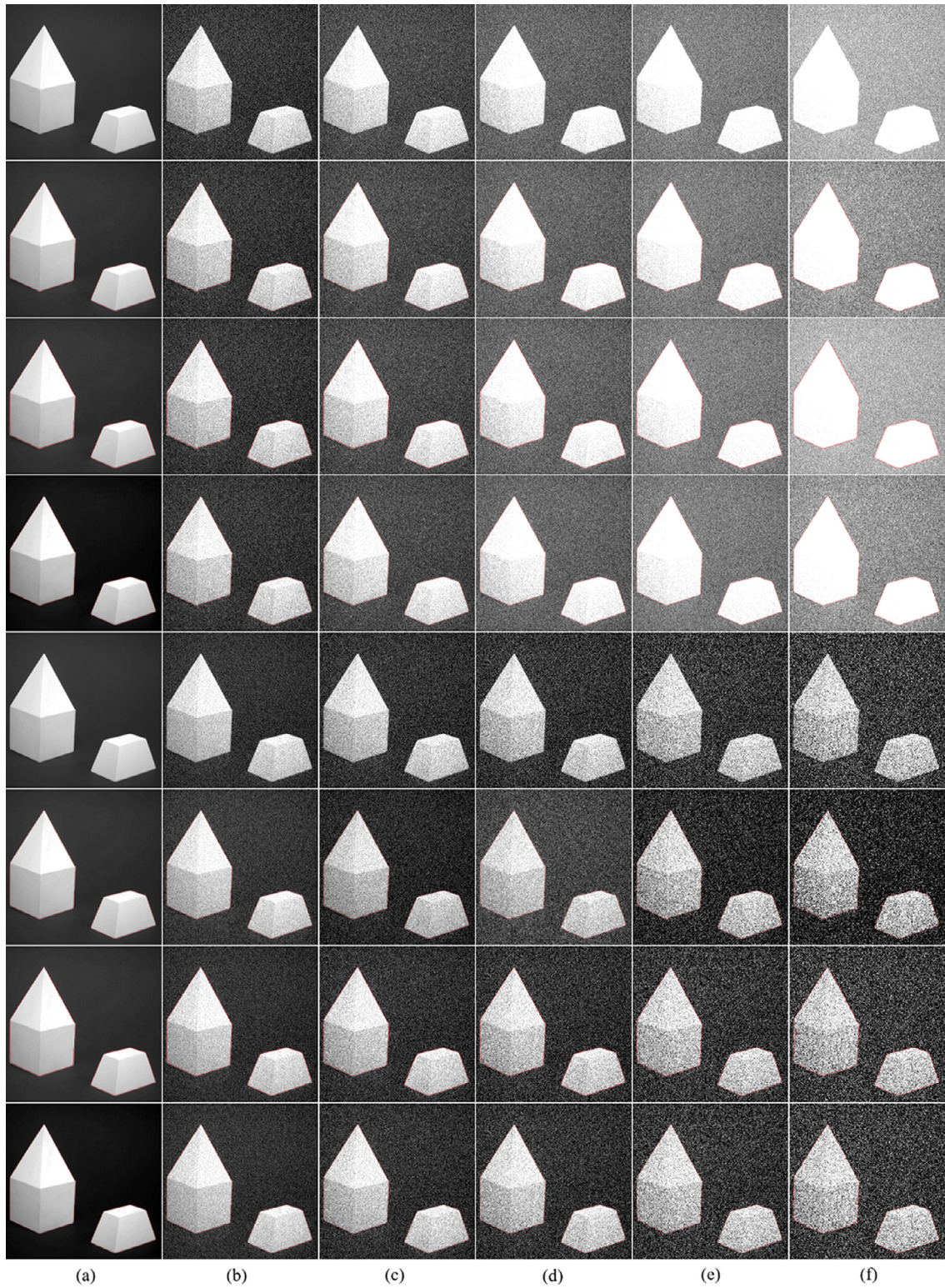
Fig. 6. Segmentation results of synthetic 3D images that are contaminated by the Gaussian white noise or random noise. The first row from the top: synthetic 3D images (from the left to the right) contaminated by the Gaussian white noise with a variance of 0.02, 0.1, 0.2, 0.3, and 0.5, respectively, and the PSNR values are 28.10, 25.72, 24.55, 24.31, and 24.29, respectively. The second to the fourth rows: segmentation results using the IRLCF, DRLSE, and LSEBFE algorithms. The fifth row: synthetic 3D images (from the left to the right) are contaminated by random noise of standard deviation of 20, 30, 40, 60, and 80, respectively; and the PSNR values are 22.09, 18.59, 16.08, 12.58, and 10.04, respectively. The sixth to the eighth rows: segmentation results using the IRLCF, DRLSE, and LSEBFE algorithms.
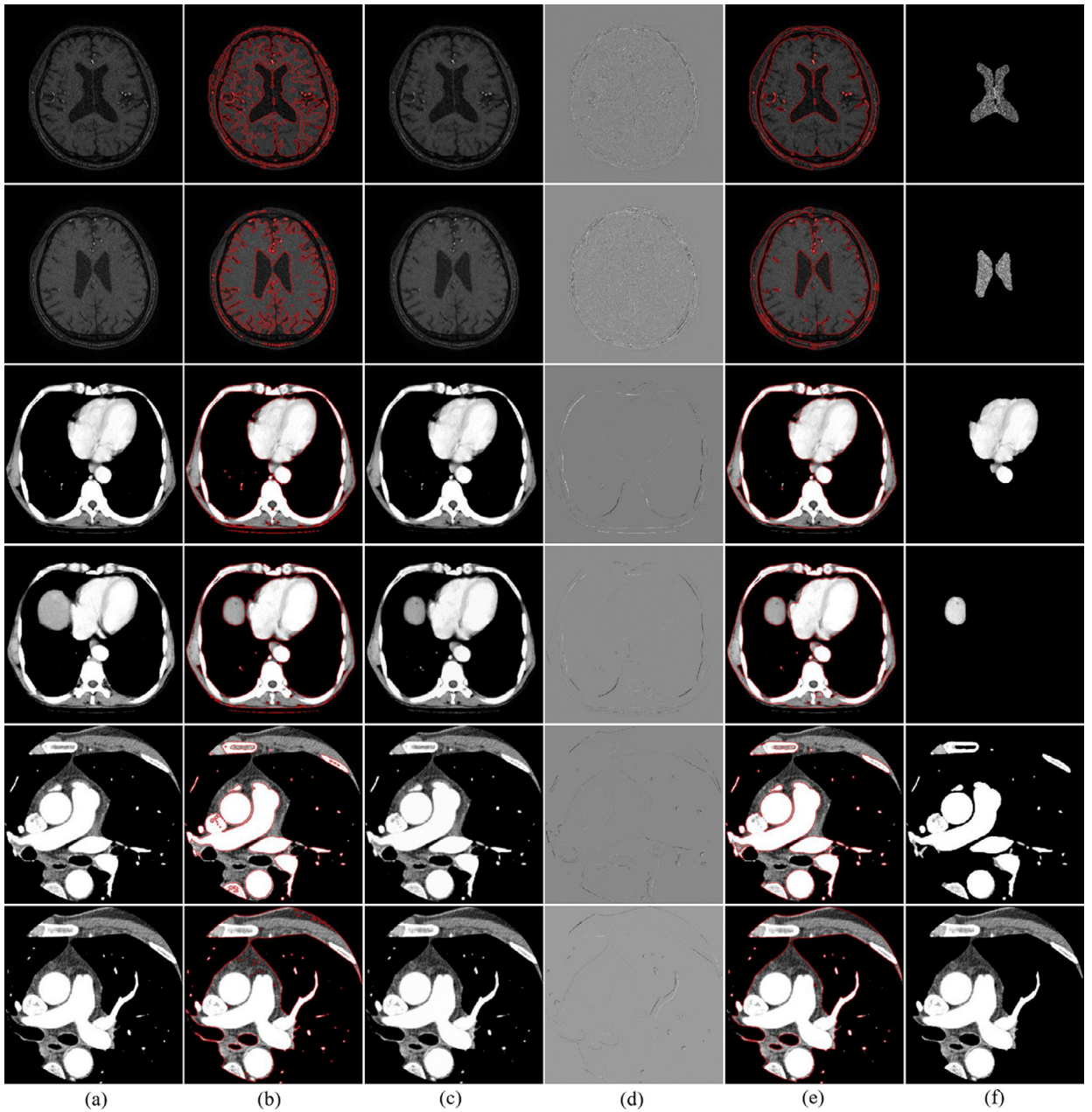
Fig. 7. The segmentation results of application of the IRLCF model to medical images. (a) (Column 1): The original images; (b) (Column 2): The initial level set contours for the image segmentation; (c) (Column 3): The recovered image; (d) (Column 4): The difference between the original image and the recovered image; (e) (Column 5): The segmentation results of the IRLCF model; and (f) (Column 6): the interested regions segmented out by the IRLCF model.

Segmentation accuracy rate (SAR) is defined as:

$$SAR = \left(1 - \frac{|R_s - T_s|}{R_s}\right) \times 100\% \tag{53}$$

where R_s represents the true area of an object, T_s is the segmented area of the object. The parameter represents occupied percentage of the image segmentation in the total area.
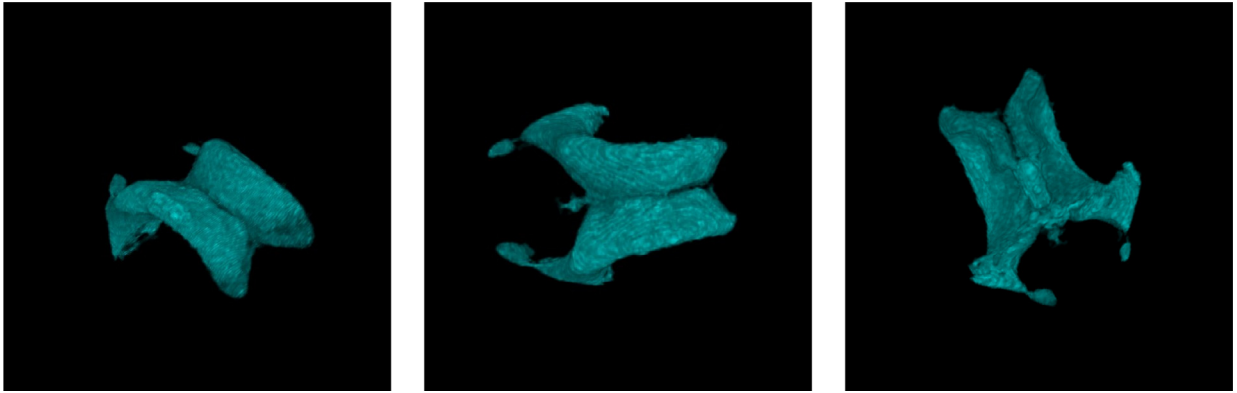
Fig. 8. The ventricle segmentation results of MRI images using the IRLCF model.

Over-segmentation rate (OSR) is defined as the ratio of the area of the pixels of the segmented objects in the segmented image that are outside the objects to be segmented to the actual total area of the objects, i.e.,

$$OSR = \frac{O_s}{R_s} \tag{54}$$

where O_s represents the area of the pixels of the segmented objects in the segmented image that are outside the objects to be segmented. It equals the area of the segmented objects in the segmented image minus the overlapped area between the segmented objects and the objects to be segmented. R_s represents the actual area of the objects.

Under-segmentation rate (USR) is defined as the area of pixels of the segmented objects in the segmented image that are inside the objects to be segmented to the actual total area of the objects, i.e.

$$USR = \frac{U_s}{R_s} \tag{55}$$

where U_s represents the area of the pixels of the segmented objects in the segmented image that are inside the objects to be segmented. It equals the true area of the objects minus the overlapped area between the segmented objects and the objects to be segmented. If the segmented objects are tumors and are used as the guide for surgery, over segmentation should be better than under segmentation.

To evaluate the segmentation accuracy, we added noises to the Heptagon, Horse, and 3D images and then performed the segmentation using the IRLCF model. The detailed evaluation results are shown in Table 2 below.

In order to overcome the shortcomings of the traditional image segmentation methods, we developed a level set model that is easy to implement and can effectively suppress noise and avoid over segmentation or under segmentation. The model can be used to segment images with different noise levels. The model can effectively suppress the noise and preserve the details of image and thus improve the quality of segmentation. These characteristics of a segmentation algorithm are very important for practical applications.

4.4. Results of experiments on medical images using the IRLCF model

As we know, there are many segmentation models that do not work well for medical images, especially for the low-level CT images and MRI images. The following medical images used for the numerical experiments are from medical imaging devices.

In order to obtain good segmentation results, we first use the fuzzy *C* mean cluster algorithm to classify the image, then we use the classified result to initialize the level set curve, which makes the level set curve closer to the boundary of the object. Results show that the proposed IRLCF model can effectively segment medical images.

In Fig. 7, the first and second rows are the low-level brain MRI images. The third and the fourth rows are the breast CT images. The fifth and the sixth rows are heart CT images. From the segmentation results we can see that the IRLCF algorithm can segment the interested inside region and locate the edge successfully although there is a slight deficiency in segmenting the outside of the image. The IRLCF model can locate the edge via the weak boundary successfully. We can see that the segmentation results are preferable, but there is also deficiency in the edge location.

In summary, the proposed IRLCF model has distinct advantages in segmenting different kinds of images in comparison to the CVMST, L0MS, and LBF models. It also has good results in segmenting practical medical images.

4.5. The ventricle segmentation of the MRI images using the IRLCF model and 3D visualization

It is generally difficult to segment brain MRI images. In the following we used the proposed IRLCF model to segment 64 brain MRI images for ventricles. The results show that the IRLCF model segments out the ventricles very accurately.

The experimental results shown in Fig. 8 are 3D visualization of the segmented images without any denoising and smoothing. We can see that the IRLCF model has good segmentation result. As to brain MRI images, the ventricle segmentation has practical applications. Doctors can judge the change of the brain cranial pressure through the change of the ventricle, then estimate the size of the brain tumor and decide to choose a conservative or an operative treatment.

5. Conclusion

In this study, we use the cosine function to express the fitting term in the traditional active contours model. Then based on the level set segmentation method, we proposed a model with partial image recovery cosine-fitting energy active contours. Experiments with different types of images, with and without noises showed that the proposed model has a strong noise immunity and can achieve better segmentation results than the CVMST, L0MS, and LBF models, but the computational speed was similar or faster than these models. Since the IRLCF model uses an image recovery method, it segments successfully the images with noise. Because the algorithm is based on the local information, it performs well in the images with intensity inhomogeneity. It is more stable and smoother than the traditional overall-fitting energy. Test results using synthetic images and real medical images show that the segmentation results are accurate and noise insensitive. Moreover, compared to the CVMST, L0MS, and LBF models, the proposed IRLCF model is more robust and efficient in segmenting intricate images.

Acknowledgments

References

[1] J.C. Bezdek, L.O. Hall, L.P. Clarke, Review of MR image segmentation techniques using pattern recognition, N Med. Phys. 20 (4) (1992) 1033–1048.
[2] X. Cai, R. Chan, T. Zeng, A two-stage image segmentation method using a convex variant of the Mumford–Shah model and thresholding, SIAM J. Imaging Sci. 6 (1) (2013) 368–390.
[3] V. Caselles, F. Catte, T. Coll, F. Dibos, A geometric model for active contours in image processing, Numer. Math. 66 (1) (1993) 1–31.
[4] V. Caselles, R. Kimmel, G. Sapiro, Geodesic active contours, Int. J. Comput. Vis. 22 (1) (1997) 61–79.
[5] R.H. Chan, M. Tao, X.M. Yuan, Constrained total variational deblurring models and fast algorithms based on alternating direction method of multipliers, SIAM J. Imaging Sci. 6 (1) (2013) 680–697.
[6] T.F. Chan, L.A. Vese, Active contours without edges, IEEE Trans. Image Process. 10 (2) (2001) 266–277.
[7] C. Chen, M.K. Ng, X.L. Zhao, Alternating direction method of multipliers for nonlinear image restoration problems, IEEE Trans. Image Process. 24 (1) (2015) 33–43.
[8] Y. Duan, H. Chang, W. Huang, et al., The regularized mumford-shah model for bias correction and segmentation of medical images, IEEE Trans. Image Process. 24 (11) (2015) 3927–3938.
[9] M.A. Figueiredo, J.M. Bioucas-Dias, R.D. Nowak, Majorization-minimization algorithms for wavelet-based image restoration, IEEE Trans. Image Process. 16 (12) (2007) 2980–2991.
[10] R. Goldenberg, R. Kimmel, E. Rivlin, M. Rudzsky, Fast geodesic active contours, IEEE Trans. Image Process. 10 (10) (2001) 1467–1475.
[11] H. Hosseini, F. Marvasti, Fast restoration of natural images corrupted by high-density impulse noise, Eurasip J. Image Video Process. 2013 15 (2013).
[12] M. Kass, A. Witkin, D. Terzopoulos, Snakes: active contour models, Int. J. Comput. Vis. 1 (4) (1988) 321–331.
[13] R. Kimmel, A. Amir, A. Bruckstein, Finding shortest paths on surfaces using level sets propagation, IEEE Trans. Pattern Anal. Mach. Intell. 17 (4) (1995) 635–640.
[14] S. Lankton, A. Tannenbaum, Localizing region-based active contours, IEEE Trans. Image Process. 17 (11) (2008) 2029–2039.
[15] C.M. Li, R. Huang, Z. Ding, C. Gatenby, D.N. Metaxas, J.C. Gore, A level set method for image segmentation in the presence of intensity inhomogeneities with application to MRI, NIEEE Trans. Image Process. 20 (7) (2011) 2007–2016.
[16] C.M. Li, C.Y. Kao, J.C. Gore, Z.H. Ding, Minimization of region-scalable fitting energy for image segmentation, IEEE Trans. Image Process. 17 (10) (2008) 1940–1949.
[17] C.M. Li, C.Y. Xu, C.F. Gui, M.D. Fox, Level set evolution without re-initialization: a new variational formulation, in: N2005 IEEE Computer Society Conference on Computer Vision and Pattern Recognition, 1, 2005, pp. 430–436.
[18] C.M. Li, C.Y. Xu, C.F. Gui, M.D. Fox, Distance regularized level set evolution and its application to image segmentation, IEEE Trans. Image Process. 19 (12) (2010) 3243–3254.
[19] J. Liu, T.Z. Huang, I.W. Selesnick, et al., Image restoration using total variation with overlapping group sparsity, Inf. Sci. 295 (C) (2015) 232–246.
[20] R. Malladi, J.A. Sethian, B.C. Vemuri, Shape modeling with front propagation: a level set approach, IEEE Trans. Pattern Anal. Mach. Intell. 17 (2) (1995) 158–175.
[21] D. Mumford, J. Shah, Optimal approximations by piecewise smooth functions and associated variational problems, Commun. Pure Appl. Math. 42 (5) (1989) 577–685.
[22] S. Osher, J.A. Sethian, Fronts propagating with curvature-dependent speed: algorithms based on hamilton-jacobi formulation, J. Comput. Phys. 79 (1) (1988) 12–49.
[23] Z.F. Pang, Y.F. Yang, A projected gradient algorithm based on the augmented lagrangian stratery for image restoration and texture extraction, Image Vis. Comput. 29 (2) (2011) 117–126.
[24] J. Park, J.M. Keller, Snakes on the watershed, IEEE Trans. Pattern Anal. Mach. Intell. 23 (10) (2001) 1201–1205.
[25] J. Pu, J. Roos, C.A. Yi, et al., Adaptive border marching algorithm: automatic lung segmentation on chest CT images, Comput. Med. Imaging Graph. 32 (6) (2008) 452–462.
[26] A. Tsai, A. Yezzi, A.S. Willsky, Curve evolution implementation of the mumford-shah functional for image segmentation, denoising, interpolation, and magnification, IEEE Trans. Image Process. 10 (8) (2001) 1169–1186.

[27] A. Vasilevskiy, K. Siddiqi, Flux-maximizing geometric flows, IEEE Trans. Pattern Anal. Mach. Intell. 24 (12) (2002) 1565–1578.
[28] L.A. Vese, T.F. Chan, A multiphase level set framework for image segmentation using the mumford and shah model, Int. J. Comput. Vis. 50 (3) (2002) 271–293.
[29] H. Wang, T.Z. Huang, Region-based object and background extraction via active contours, Opt. Int. J. Light Electron Opt. 124 (23) (2013) 6020–6026.
[30] H. Wang, T.Z. Huang, An adaptive weighting parameter estimation between local and global intensity fitting energy for image segmentation, Commun. Nonlinear Sci. Numer. Simul. 19 (9) (2014) 3098–3105.
[31] H. Wang, T.Z. Huang, Y.Q. Du, A global minimization hybrid active contour model with applications to oil spill images, Computers & Mathematics with Applications 68 (3) (2014) 353–362.
[32] H. Wang, T.Z. Huang, Z. Xu, Y.G. Wang, An active contour model and its algorithms with local and global gaussian distribution fitting energies, Inf. Sci. 263 (1) (2014) 43–59.
[33] H. Wang, T.Z. Huang, Z. Xu, Y.G. Wang, A two-stage image segmentation via global and local region active contours, Neurocomputing 205 (C) (2016) 130–140.
[34] Y.G. Wang, T.Z. Huang, H. Wang, Region-based active contours with cosine fitting energy for image segmentation, J. Opt. Soc. Am. Opt. Image Sci. Vis. 32 (11) (2015) 2237–2246.
[35] Y. Xiang, A.C.S. Chung, J. Ye, An active contour model for image segmentation based on elastic interaction, J. Comput. Phys. 219 (1) (2006) 455–476.
[36] C.Y. Xu, J.L. Prince, Nakes, shapes, and gradient vector flow, IEEE Trans. Image Process. 7 (3) (1998) 359–369.
[37] Z. Xu, T.Z. Huang, H. Wang, C.L. Wang, Variant of the region-scalable fitting energy for image segmentation, J. Opt. Soc. Am. Opt. Image Sci. Vis. 32 (3) (2015) 463–470.
[38] M. Yan, Estoration of images corrupted by impulse noise and mixed gaussian impulse noise using blind inpainting, SIAM J. Imaging Sci. 6 (3) (2013) 1227–1245.
[39] X.L. Zhao, F. Wang, M.K. Ng, A new convex optimization model for multiplicative noise and blur removal, SIAM J. Imaging Sci. 7 (1) (2014) 456–475.